NASA/TM—2012-217219

Computational Analyses of the LIMX TBCC Inlet High-Speed Flowpath

Vance F. Dippold, III
Glenn Research Center, Cleveland, Ohio

January 2012

NASA STI Program . . . in Profile

Since its founding, NASA has been dedicated to the advancement of aeronautics and space science. The NASA Scientific and Technical Information (STI) program plays a key part in helping NASA maintain this important role.

The NASA STI Program operates under the auspices of the Agency Chief Information Officer. It collects, organizes, provides for archiving, and disseminates NASA's STI. The NASA STI program provides access to the NASA Aeronautics and Space Database and its public interface, the NASA Technical Reports Server, thus providing one of the largest collections of aeronautical and space science STI in the world. Results are published in both non-NASA channels and by NASA in the NASA STI Report Series, which includes the following report types:

- TECHNICAL PUBLICATION. Reports of completed research or a major significant phase of research that present the results of NASA programs and include extensive data or theoretical analysis. Includes compilations of significant scientific and technical data and information deemed to be of continuing reference value. NASA counterpart of peer-reviewed formal professional papers but has less stringent limitations on manuscript length and extent of graphic presentations.

- TECHNICAL MEMORANDUM. Scientific and technical findings that are preliminary or of specialized interest, e.g., quick release reports, working papers, and bibliographies that contain minimal annotation. Does not contain extensive analysis.

- CONTRACTOR REPORT. Scientific and technical findings by NASA-sponsored contractors and grantees.

- CONFERENCE PUBLICATION. Collected papers from scientific and technical conferences, symposia, seminars, or other meetings sponsored or cosponsored by NASA.

- SPECIAL PUBLICATION. Scientific, technical, or historical information from NASA programs, projects, and missions, often concerned with subjects having substantial public interest.

- TECHNICAL TRANSLATION. English-language translations of foreign scientific and technical material pertinent to NASA's mission.

Specialized services also include creating custom thesauri, building customized databases, organizing and publishing research results.

For more information about the NASA STI program, see the following:

- Access the NASA STI program home page at *http://www.sti.nasa.gov*

- E-mail your question via the Internet to *help@sti.nasa.gov*

- Fax your question to the NASA STI Help Desk at 443–757–5803

- Telephone the NASA STI Help Desk at 443–757–5802

- Write to:
  NASA Center for AeroSpace Information (CASI)
  7115 Standard Drive
  Hanover, MD 21076–1320

NASA/TM—2012-217219

Computational Analyses of the LIMX TBCC Inlet High-Speed Flowpath

Vance F. Dippold, III
Glenn Research Center, Cleveland, Ohio

Prepared for the
58th Joint Army-Navy-NASA-Air Force (JANNAF) Propulsion Meeting
sponsored by the JANNAF Interagency Propulsion Committee
Arlington, Virginia, April 18–22, 2011

National Aeronautics and
Space Administration

Glenn Research Center
Cleveland, Ohio 44135

January 2012

Acknowledgments

This work was supported by the Fundamental Aeronautics Hypersonics Project.
The author is grateful for the help of J. Dave Saunders, John Slater, Bobby Sanders, and Lois Weir.

This work was sponsored by the Fundamental Aeronautics Program at the NASA Glenn Research Center.

Level of Review: This material has been technically reviewed by technical management.

Available from

NASA Center for Aerospace Information
7115 Standard Drive
Hanover, MD 21076–1320

National Technical Information Service
5301 Shawnee Road
Alexandria, VA 22312

Available electronically at http://www.sti.nasa.gov

Computational Analyses of the LIMX TBCC Inlet High-Speed Flowpath

Vance F. Dippold, III
National Aeronautics and Space Administration
Glenn Research Center
Cleveland, Ohio 44135

Abstract

Reynolds-Averaged Navier-Stokes (RANS) simulations were performed for the high-speed flowpath and isolator of a dual-flowpath Turbine-Based Combined-Cycle (TBCC) inlet using the Wind-US code. The RANS simulations were performed in preparation for the Large-scale Inlet for Mode Transition (LIMX) model tests in the NASA Glenn Research Center (GRC) 10- by 10-ft Supersonic Wind Tunnel. The LIMX inlet has a low-speed flowpath that is coupled to a turbine engine and a high-speed flowpath designed to be coupled to a Dual-Mode Scramjet (DMSJ) combustor. These RANS simulations were conducted at a simulated freestream Mach number of 4.0, which is the nominal Mach number for the planned wind tunnel testing with the LIMX model. For the simulation results presented in this paper, the back pressure, cowl angles, and freestream Mach number were each varied to assess the performance and robustness of the high-speed inlet and isolator. Under simulated wind tunnel conditions at maximum inlet mass flow rates, the high-speed flowpath pressure rise was found to be greater than a factor of four. Furthermore, at a simulated freestream Mach number of 4.0, the high-speed flowpath and isolator showed stability for freestream Mach number that drops 0.1 Mach below the design point. The RANS simulations indicate the yet-untested high-speed inlet and isolator flowpath should operate as designed. The RANS simulation results also provided important insight to researchers as they developed test plans for the LIMX experiment in GRC's 10- by 10-ft Supersonic Wind Tunnel.

Nomenclature

D	flowpath cross-section diameter; in.
M	Mach number
p	static pressure; psi
Re_x	Reynolds number per foot
T	static temperature; °R
u	streamwise velocity; ft/s
x	streamwise distance from leading edge of trapezoidal plate; in.
y^+	non-dimensional wall distance

Subscripts

AIP	Aerodynamic Interface Plane
CFD	from computational fluid dynamics (CFD) simulations
COR	corrected to account for first turn shock loss in true Mach 4 freestream flow
eq	equivalent
iso	isolator entrance
ref	reference condition, no-back pressure
t	throat of convergent-divergent section
0	total condition
∞	freestream condition

Introduction

Air-breathing hypersonic flight has been a focus of aeronautics research for the past half century (Refs. 1 and 2). NASA has invested in air-breathing hypersonic flight because it is an intriguing alternative method for reaching low earth orbit and access to space rather than using conventional rocket propulsion systems (Refs. 1 and 3). The advantage of air-breathing hypersonic propulsion systems over rocket systems is that the air-breathing systems carry only their fuel and use the oxygen present in the atmosphere as the oxidizer, thus reducing the total take-off weight and the cost.

A focal point for air-breathing hypersonic propulsion is a Dual Mode Scramjet (DMSJ) combustor (Ref. 4). However, unlike conventional turbine engines, DMSJ-based propulsion systems require forward velocity to produce thrust. Thus, systems have been developed to accelerate these vehicles from take-off to speeds in which the DMSJ propulsion system can operate effectively (typically upwards of Mach 3 to 4). Rocket-Based Combined-Cycle (RBCC) systems use rockets engines to boost the vehicle to the Mach 3 to 4 range, at which time the ramjet and scramjet engine can begin operating (Ref. 5). Turbine-Based Combined-Cycle (TBCC) systems use turbine engines to accelerate the vehicle to the ramjet transition velocity (Ref. 6).

While ramjet- and scramjet-enabling technologies have been developed over many decades, few studies have focused on how to effectively transition from the turbine stage to DMSJ stage—this critical event is referred to as Mode Transition. The NASA Fundamental Aeronautics Program is conducting experiments with a Large-scale Inlet for Mode Transition (LIMX) (Refs. 7 and 8) to map out and demonstrate the process of transitioning from the turbine to the DMSJ stages of a TBCC system. These tests will be conducted in NASA Glenn Research Center's (GRC) 10- by 10-ft Supersonic Wind Tunnel (Ref. 9). The LIMX inlet is an over-under inlet that consists of a low-speed flowpath for a turbine engine and a high-speed flowpath with an isolator that could be coupled to a DMSJ engine. Moving ramps and cowls vary the shape of the inlet so it can operate over a range of freestream conditions (Ref. 10). The low-speed flowpath includes bleed regions to help control and optimize the flow entering the engine face. During the initial phases of testing, mass-flow plugs will be used to back-pressure each flowpath, simulating an actual engine; in later phases of testing, an actual turbine engine will be coupled to the low-speed flowpath. A rotating cowl between the low-speed and high-speed flowpaths is used to split the inlet flow into two directions—low-speed and high-speed flowpaths. This rotating cowl is also referred to as the inlet splitter. The splitter can be positioned to close off flow through the low-speed flowpath and direct flow into the high-speed flowpath. The high-speed flowpath consists of a rectangular inlet and a rectangular-to-round isolator upstream from where a DMSJ combustor would be located. The isolator has an area increase of 20 percent and length-to-diameter of 7.2, in which the diameter is based on the diameter of a circle equivalent in area to the throat of the high-speed flowpath. The high-speed flowpath was designed to be coupled to an actual DMSJ combustor. However, for economical reasons, current test plans will only use a cold-pipe and massflow plug assembly to back-pressure this flowpath.

Small-scale experimental tests were performed in GRC's 1- by 1-ft Supersonic Wind Tunnel to validate the design of the low-speed flowpath (Ref. 7). The massflow and back pressure performance of the low-speed flowpath was assessed and optimized by adjusting the bleed rates and region sizes for a range of cowl angles and back pressure conditions. While the small-scale Inlet for Mode Transition (IMX) model did include a high-speed flowpath, this flowpath did not include the rectangular-to-round isolator or a means to back-pressure the high-speed flowpath. Therefore, no data is available from the IMX experiments to validate computational fluid dynamics (CFD) results for the high-speed flowpath. These two shortcomings are not true for the LIMX model. Therefore, CFD simulations were performed for the LIMX high-speed flowpath to computationally predict the flow characteristics through the high-speed flowpath, especially the back pressure performance of the yet-untested rectangular-to-round isolator. Additionally, the CFD simulations were performed in order to predict the stability of the inlet in the event the high-speed Mach number decreased.

The rectangular-to-round isolator experiments associated with the LIMX hardware will also provide a new data set. Due to the geometry of the LIMX inlet, which was designed to model an actual installed

TBCC inlet, the isolator in the LIMX test will see asymmetric inflow. For example, the boundary layer on the ramp side is expected to be much thicker than the boundary layer on the cowl side due to the far greater distance the flow travels over the ramp to the isolator. While a number of past studies have looked at isolators with asymmetric inflows, most used two-dimensional isolators (Ref. 11). Few past efforts have considered rectangular-to-round isolators with asymmetric inflows (Ref. 12), and the LIMX experiments and CFD simulations will help broaden the range of available data.

The CFD simulations will help researchers understand and interpret the experimental results once experimental data becomes available.

Modeling

LIMX Experimental Model

The LIMX inlet model is a dual-stream inlet system with a low-speed flowpath designed to be coupled to a turbine engine and a high-speed flowpath designed to be coupled to a DMSJ combustor (Ref. 10). A computer automated design (CAD)-generated image of the LIMX design, as it will be installed in GRC 10- by 10-ft Supersonic Wind Tunnel, is illustrated in Figure 1. The overall length of the model, from tip to tail, is nearly 30 ft, and the width of the inlet flowpaths is 12 in. The two flowpaths are arranged in an over-under configuration, separated by a rotating splitter. Figure 2 shows the dual-flowpath inlet system with the splitter positioned to allow flow into both flowpaths. The low-speed flowpath is a Mach 4 design—the upper limit of the target mode-transition window—while the high-speed flowpath is a Mach 7 design. During the inlet mode transition, the splitter rotates toward the low-speed flowpath ramp surface to fully close off the low-speed flowpath. Since this work focuses on the high-speed flowpath, the reader is directed to References 7, 8, and 10 for more details concerning the low-speed flowpath.

The LIMX model is supported from the top by a strut in the wind tunnel, as shown in Figure 1. A schematic of the LIMX high-speed flowpath is shown in Figure 3. Freestream air first encounters the model at the tip of a large trapezoidal precompression forebody plate, which has a ramp angle of 6.5°. In addition to the trapezoidal plate, the ramp turns another 6°, 77.95 in. downstream of the leading edge. At this turn, the sidewall begins, with a 20° leading edge angle. Using the leading edge of the trapezoidal plate as the reference point, x=0 in., the flow for the high-speed flowpath compresses again on the back of the splitter another 7° at x=111.72 in. Before encountering the high-speed cowl tip, the high-speed flow undergoes 19.5° of total compression. Inside the inlet, at x=156.70 in., the flow along the ramp experiences an 8.5° expansion turn. This results in 11° of combined compression. The two-dimensional, rectangular high-speed flowpath entrance is nominally 141.56 in. downstream from the leading edge and it has a nominal capture height of 32.957 in. The high-speed inlet cowl can rotate from +2° (away from the ramp) to –11° (towards the ramp). The high-speed flowpath throat is located at station x=181.0 in. and has a height of 2.50 in. The isolator is positioned downstream of the inlet throat. The rectangular-to-round isolator has a 20 percent area increase. Using the diameter of a circle of equivalent area as the isolator entrance ($D_{eq,iso}$), the length of the isolator was designed to be $7.2*D_{eq,iso}$. The aerodynamic interface plane (AIP) is located at the end of the isolator, at x=225.43, and has a diameter of 6.60 in. The AIP represents the entrance to a DMSJ combustor. However, the current experimental test plans do not include testing with a DMSJ combustor. Instead, a cold pipe with a conical massflow plug will be connected downstream of the isolator to impose back pressure upon the high-speed flowpath.

The high-speed flowpath was designed for Mach 7 freestream conditions; however most of the inlet mode-transition testing will be conducted at Mach 4, which is near the low-speed flowpath design point and the mode-transition freestream Mach number. While the LIMX model's mode-transition Mach number is Mach 4, the 10- by-10-ft Supersonic Wind Tunnel is limited to Mach 3.5101 with proper temperature and pressure conditions. To overcome this limitation, the LIMX model will be rotated to a –6.856° angle-of-attack such that the throat Mach numbers will be representative of what would be expected if Mach 4 conditions were available to the model (Ref. 13). Therefore, while the actual wind

tunnel Mach number is 3.5101. This configuration is referred to as simulated Mach 4. Tunnel conditions will be set to a total pressure of 35.970 psi and a Reynolds number of Re_x=2.55 million.

Computational Model

The Wind-US code, version 2.0 (Refs. 14 and 15), was used to run the CFD simulations of the LIMX high-speed flowpath. The Wind-US code is a general-purpose, Reynolds-Averaged Navier-Stokes (RANS) CFD solver for both structured and unstructured grids. The code is developed and managed by the NPARC Alliance, a partnership between GRC, U.S. Air Force Arnold Engineering Development Center, and The Boeing Company. The Wind-US code offers several numerical schemes, as well as several zero-, one-, and two-equation turbulence models. The Wind-US code includes the second-order Roe numerical scheme and the Menter Shear Stress Transport (SST) turbulence model (Ref. 16) which were used for this study. The CFD simulations were performed on various multi-node Linux (Linus Torvalds) clusters, typically using eight to 20 processor cores. Even so, the simulations took four to seven days of wall-clock time to converge.

Structured grids were created for the LIMX high-speed flowpath. It should be noted that the computational grids were constructed for the LIMX model in an upside-down configuration, like Figure 2. These grids took advantage of several assumptions to simplify the simulation in an effort to reduce the computational expense. First, horizontally symmetric flow was assumed since the inlet model is horizontally symmetric. The grid was created for only half the inlet, using an inviscid wall boundary condition along the symmetry plane. Second, the low-speed flowpath was assumed to have no effect on the high-speed flow when the splitter is positioned to fully close-off the low-speed flowpath. Therefore, only the high-speed flowpath was modeled. Third, it was assumed that spillage over the inlet sidewalls would be nearly zero since the sidewalls are designed to be well forward of the oblique shock location. Under this assumption, only the flow immediately upstream of the inlet and sidewalls was modeled—the full trapezoidal plate of the experimental model was not simulated—and inviscid wall boundary conditions were imposed along the grid surfaces upstream of the inlet sidewall. Lastly, it was assumed that the cold pipe and mass flow plug downstream of the high-speed isolator could be simulated by a convergent-divergent section as a way to impose back pressure. The throat area of the convergent-divergent section would be variable to create a desired back pressure. Modeling a convergent-divergent section would be significantly simpler than creating a grid for the mass flow plug. The convergent-divergent section was placed two AIP diameters downstream of the AIP. The throat area of this convergent-divergent section was reduced to increase back pressure through the high-speed flowpath. For the cases presented here, the convergent-divergent throat areas ranged from 100 to 73 percent of the AIP area.

In the streamwise direction, the grid had 481 points along the ramp, 161 points spaced through the high-speed inlet, and 201 points spaced through the isolator. The maximum streamwise spacing through each of these sections was 0.59 in. inside the inlet and isolator, and 1.46 in. overall. There were 81 points placed vertically across the flowpath and 45 points placed horizontally across the flowpath. The grid was packed to viscous walls, such that the grid spacing at the wall was nominally set to a non-dimensional wall spacing of y^+=0.5. It has been shown that the non-dimensional wall spacing, y^+, of the first grid point off the wall needs to be on the order of 1.0 (Refs. 17 and 18). Each grid had 4.5 million grid points. The typical grid is shown in Figure 4.

The inflow into the computation uses the frozen inflow boundary condition, which fixes the Mach number, static pressure, static temperature, and flow angle at the inflow and is applicable to supersonic inflows because changes in the flow properties downstream do no propagate upstream (Ref. 19). The wind tunnel test section conditions were specified at the inflow: M_∞=3.5101, p_∞=0.46446 psi, and T_∞=222.506 °R. The flow angle was set to 6.856°, as previously mentioned, to simulate a Mach 4 freestream flow. (The angle-of-attack was positive in the RANS simulations, since the model was upside-down compared to the experiment.) At the outflows, since the flow there would likely be supersonic, no pressure boundary condition was imposed. Instead, the flow properties were extrapolated on the boundary.

To speed up convergence of each solution, each grid was run using every fourth grid point, and then every second grid point, before finally converging the solution using every grid point. Solving on the coarser grids first allowed the overall flowfield to set up rather quickly before solving the turbulence details in the finest grid. This approach is standard practice for structured RANS calculations and is commonly referred to as grid sequencing. Furthermore, converging the solution on multiple grid sequence levels helped ensure that the finest grid solution was not dependent on the grid (i.e., the solution would not change significantly if minor changes to the grid were made). Table 1 shows the massflow and mass-averaged total pressure at the AIP for the coarse (every fourth grid point), medium (every second grid point), and fine grid solutions. The mass-averaged total pressure is defined as:

$$\text{Mass-averaged total pressure} = \frac{\int_A (p_0 \cdot \rho \cdot u) dA}{\int_A (\rho \cdot u) dA}$$

in which p_0 is the local total pressure, u is the local streamwise velocity, ρ is the local density, and A is the cross-section area. Table 1 also shows the percent difference in the massflow and mass-averaged total pressure between the three grid sequence solutions. Between the coarse and medium grid solutions, the massflow differs by 1.15 percent and the total pressure differs by 2.56 percent. Between the medium and fine solutions, the differences are 0.55 and 0.63 percent, respectively. This large reduction in percent difference shows that the solution is reaching grid-independence for the fine grid.

Lastly, each solution was started from the default, freestream-flow initialization by Wind-US. While the grid topologies were identical and solutions could be restarted from solutions of different cowl angles and back pressure configurations, comparisons during early simulations indicated that hysteresis existed. For the same back-pressured configuration, the RANS solver converged to different solutions for increasing back pressure cases (restarting from a solution with a larger convergent-divergent throat area) and decreasing back pressure cases (restarting from a solution with a smaller convergent-divergent throat area). Therefore, it was decided to begin all simulations from the same solution initialization—freestream conditions, the Wind-US default initialization.

Results

No Back Pressure Applied

The first set of simulated LIMX high-speed flowpath cases that was run varied the high-speed cowl angle and did not back-pressure the inlet, i.e., the convergent-divergent throat area was 100 percent of the AIP area. For these cases, the high-speed cowl was rotated from –11° to +2° (fully open). The computed massflow rate at the AIP is plotted with respect to high-speed cowl rotation angle in Figure 5. As the cowl angle increases from –11° to –5°, the massflow rate increases and eventually peaks. However, after the massflow rate peak at –5° cowl angle, it is decreased at the –4° cowl angle. From –4° cowl angle to 0° cowl angle, the massflow rate further decreases. From 0° to +2° cowl angle, the massflow into the high-speed AIP sharply decreases, and it is believed that the inlet is unstarted in this configuration. While the high-speed inlet was designed to achieve maximum massflow with a 0° cowl angle at the Mach 7 design point (Ref. 10), the numerical simulations indicate that the massflow peaks at a –5° cowl angle for the Mach 4 mode transition point. This prediction will help test planners to concentrate measurements at the –5° cowl angle to maximize inlet performance during mode.

The CFD simulations predict that a massflow rate maximum exists at –5° cowl rotation. It is important to understand how the inlet behaves at larger cowl angles, especially if it does experience unstart. In Figure 6, signed Mach number (sign(u)*M) contours are plotted at the high-speed flowpath entrance, x=141.56. A negative Mach number indicates that the flow direction is upstream. At the smaller cowl angles (–11°, –9°, –6°, and –5°), the flow into the high-speed inlet remains attached, though the boundary layer is noticeably thicker along the ramp surface than along the cowl surface, especially at the

corners. However, at cowl angles of –4° and larger, large regions of separated flow exist along the ramp corners. In Figure 7, Mach number contours are plotted at cross sections spaced 2 in. apart along the high-speed flowpath. Looking at the solutions for cowl angles of 0° to –4°, the large regions of separated flow (denoted by the dark blue iso-surfaces) in the corners extend up to 10 in. into the high-speed flowpath. While separated flow is observed along the ramp and the ramp corners in the –5° to –9° cowl angle solutions, it does not encompass nearly as large a percentage of the cross sectional area as for 0° to –4° cowl angle solutions. These regions of large separated flow impose a blockage on the inlet, reducing the aerodynamic capture area, and thereby causing the reduction in massflow observed in Figure 6 for cowl angles of 0° to –4° (Ref. 13).

Similar to Figure 7, Figure 8 shows the Mach number contours at cross sections, equally spaced every 4 in., along the compression ramp forward of the high-speed cowl tip (x<141 in.), at the inlet entrance, and aft of the cowl tip (x> 141 in.) of the high-speed flowpath for each cowl angle. The plots also include streamlines extending forward from the cowl leading edge that loosely depict the stream tube flowing into the high-speed flowpath. For the cowl angles of –5° and less, the stream tube is mostly flat in the vertical direction (i.e., the stream traces have constant y-values at each cross section) far upstream of the flowpath entrance. For the cowl angles of –4° and greater, the stream tube curls down in the vertical direction near the inlet sidewall. This further illustrates the reduced upstream capture area flowing into the high-speed flowpath. This inlet does not appear to be unstarted in the traditional definition, in which the pressure rise moves upstream of the inlet entrance. However, this inlet is considered to be unstarted because the captured massflow is reduced due to aerodynamic blockage at the entrance, caused by the massive corner separations (Ref. 11). The non-back-pressured inlet analyses predict that maximum massflow configuration of the high-speed flowpath is with the high-speed cowl angle set within the following range: –4° to –6°.

Back Pressure Applied

Upon determining the range of high-speed flowpath cowl rotation angles that maximized massflow (–4° to –6°), the high-speed flowpath was back-pressured to simulate the presence of a DMSJ combustor. In the LIMX tunnel experiment, a cold-pipe and massflow plug assembly will be used to vary back pressure. Following the convention used by Slater and Saunders (Ref. 20), in an effort to reduce computational complexity and solution time, a converging-diverging nozzle section with a variable throat area downstream of the AIP was used to vary back pressure. The throat areas ranged from 75 to 90 percent of the AIP cross section area.

The maximum massflow into the LIMX high-speed flowpath, without back pressure, was achieved with the simulation configured with a cowl rotation angle of –5°. Next, this configuration was simulated again with a back pressure that varied within the range from $p_{AIP}/p_{iso,ref}$=0.781 to $p_{AIP}/p_{iso,ref}$=2.86. The reference pressure condition, $p_{iso,ref}$, is the mass-averaged static pressure at the isolator entrance for the non-back-pressured condition; the AIP pressure, p_{AIP}, is the mass-averaged static pressure at the AIP. Figure 9 shows six simulation results with axial distributions of ramp and cowl surface pressures plots and numerical-schlieren plots through the isolator. Each simulation pertained to a unique back pressure state. Immediately noticeable is the waviness of the cowl surface pressure plots compared to the relatively smooth ramp surface pressure plots. Along the cowl surface, shock and expansion waves are clearly observed; whereas along the ramp surface only a smooth pressure rise is observed after an initial shock. While this difference in pressure rise along the isolator surfaces may initially be puzzling, it is quite understandable when put into the context of an asymmetric flowpath: due to a greater ramp length than cowl length, a thick boundary layer forms along the ramp surface. The shock and expansion waves easily penetrate the thin boundary layer on the cowl, but they do not fully transmit through the thick boundary layer along the ramp (Ref. 8). This is observed in the numerical-schlieren images in Figure 9, especially for $p_{AIP}/p_{iso,ref}$=1.62, 2.28, and 2.72, in which the dark regions depicting the shock waves do not fully extend to the lower ramp surface. Therefore, only a smooth pressure rise is observed along the ramp surface.

Another interesting feature observed in the pressure plots of Figure 9 is that it is quite feasible to back-pressure the flowpath upstream of the isolator. While convention typically limits back-pressuring the flowpath to only the isolator, the simulations show that the downstream region of the inlet section can be back-pressured, too, and remain stable. During the experimental testing of this inlet, while the isolator is fully back-pressured (in the range of $p_{AIP}/p_{iso,ref}$=2.72), the CFD simulations predict that the high-speed flowpath can withstand at least an additional 14 percent increase in back pressure (with respect to the reference isolator entrance pressure) without unstarting. This is quite important to the safety of the model, the safety of the wind tunnel facility, and the efficiency of the test program. If a similar inlet and isolator design were to be used in a flight vehicle, this additional unstart margin would help increase mission safety as well.

The LIMX high-speed flowpath was also back-pressured for cowl angles of –4° and –6°. For these simulations, the isolator pressure had the following ranges:

- For the –4° cowl angle, $p_{AIP}/p_{iso,ref}$ = 0.728 to 2.27.
- For the –6° cowl angle, $p_{AIP}/p_{iso,ref}$ = 0.841 to 3.46.

Figures 10 and 11 show the surface pressure and numerical-schlieren plots for the back-pressured –4° and –6° cowl angle inlets. As with the –5° cowl angle configuration that had results plotted in Figure 9, the boundary layer along the ramp surface is significantly thicker than that along the cowl surface. Again, this causes a smooth pressure rise on the ramp surface, whereas the shock and expansion waves are clearly observed in the pressure plots along the cowl surface. The CFD simulations predict that the –4° cowl configuration with a fully back-pressured isolator ($p_{AIP}/p_{iso,ref}$=2.18) can withstand at least a nine percent increase in pressure (with respect to the isolator reference pressure) before the inlet unstarts. Similarly, the –6° cowl configuration with a fully back-pressured isolator ($p_{AIP}/p_{iso,ref}$=3.17) can experience at least a 29 percent increase in pressure before the inlet unstarts. These results show that the high-speed inlet and isolator can be stably back-pressured through the –4° to –6° range of cowl angles.

Another way to quantify the isolator performance is to compare the pressure rise through the isolator to the normal shock pressure rise for the same inflow (Ref. 18). Tables 2 to 4 list the pressure rise through the isolator as a percentage of the normal shock pressure rise for each of the three back-pressured configuration of the LIMX high-speed flowpath, using the corresponding non-back-pressured configuration (high-speed cowl angle) as the reference. The table also lists the AIP total pressure as a percentage of the normal shock total pressure. For the fully back-pressured, –4° cowl angle configuration ($p_{AIP}/p_{iso,ref}$=2.18), the isolator attains 96.6 percent of the static pressure rise of the normal shock and maintains 89.7 percent of the normal shock total pressure. For –5° ($p_{AIP}/p_{iso,ref}$=2.72) and –6° ($p_{AIP}/p_{iso,ref}$=3.17) cowl angles, the isolator attains 90.0 and 89.6 percent of the normal shock pressure rise, and maintains 82.9 and 84.0 percent of the normal shock total pressure.

In addition to observing the calculated surface pressure and numerical-schlieren plots for the back-pressured high-speed flowpath, it was helpful to look at Mach number contours through the isolator. Figure 12 shows Mach number cross section contour plots equally spaced every 2 in. through the isolator for the fully back-pressured isolator and for each high-speed cowl angle. These plots show that the flow in the high-speed flowpath separates from the ramp surface (indicated by the blue iso-surface) upstream of the isolator but reattaches in the upstream half of the isolator—far upstream of the AIP. The plots also show that a thick boundary layer develops along the ramp surface. While the flow decelerates considerably from the beginning of the isolator to the AIP, from near Mach 2 local flow to barely sonic local flow, the flow is not uniform as it passes the AIP, primarily due the difference in boundary layer thickness between the ramp and cowl surfaces. The non-uniformity of the flow at the AIP is further observed in contour plots of Mach number in Figures 13 to 15. Without back pressure, the core flow through the isolator exceeds Mach 1.8 (for the –4° cowl angle) to Mach 2.2 (for the –6° cowl angle). In the thick boundary layer along the ramp, the flow reduces to Mach 1.2 to Mach 1.4 above the wall. When the isolator is fully back-pressured, the AIP sees a core Mach number between 0.8 and 1.0 while the flow is Mach 0.2 to 0.3 near the bottom of the thick boundary layer. Pressure, normalized by the freestream

static pressure, is similarly plotted in Figures 16 to 18. The AIP pressure contour plots show that the pressure is also non-uniform across the AIP, as one might expect. In most configurations, the static pressure is greater on the cowl side of the high-speed flowpath at the AIP than on the ramp side. For turbine flowpaths, this non-uniform pressure distribution is quantified as the static pressure distortion: $(p_{max} - p_{min})/p_{avg}$ (Ref. 8). The static pressure distortion at the AIP is listed in Tables 2 to 4. For the fully back-pressured isolator, the static pressure distortion at the AIP ranges from 8.9 percent for cowl angles of 5° and 6° to 10.1 percent for a cowl angle of 4°. While the static pressure distortion is a useful figure of merit for turbine-based inlets, it is unclear how useful it is for a DMSJ combustor, in which there are no moving parts to stall or fatigue.

Inflow Mach Number Stability

The –6° cowl angle configuration was further tested for freestream Mach number stability. Using the back-pressured case $p_{AIP}/p_{iso,ref}$=3.17, the simulated freestream Mach number was reduced from Mach 4 to 3.9. (This corresponded to a reduction of actual tunnel Mach number from Mach 3.5101 to 3.4293). A plot of the surface pressure is shown in Figure 19. Due to the lower freestream total pressure, the pressure rise in the high-speed flowpath moves forward from the beginning of the isolator (black trace) to about 6 in. upstream of the isolator (red trace). Since the CFD simulation predicted that the high-speed flowpath would remain stable at Mach 3.9, the freestream simulated Mach number was further reduced, to Mach 3.8 (Mach 3.3458, actual). In this case, the CFD simulation did not converge, as the high-speed flowpath lost back pressure and unstarted. These two simulations predict that the high-speed flowpath had a simulated freestream Mach number margin of 0.1 Mach, agreeing with the inlet design (Ref. 8).

Future Work

In the future, after data from the first phases of the LIMX tests are available, the experimental data will be compared to the simulation results reported here. The experimental data will be used to validate and improve the computer code and the methods for computational analysis of hypersonic inlets and isolators. Lastly, upon successfully validating the computational results with the experimental data, validated simulation results will also be used to help clarify the experimental results—fill in the gaps in regions of the high-speed flowpath where experimental data isn't available. In this way, both the numerical prediction of high-speed flow paths and understanding of mode transition are improved.

Conclusions

In preparation of the Large-scale Inlet for Mode Transition (LIMX) tests in the NASA Glenn Research Center's 10- by 10-ft Supersonic Wind Tunnel, high-fidelity, numerical simulations were performed for the LIMX high-speed flowpath using the Wind-US computational fluid dynamics (CFD) code. The high-speed flowpath is part of an over-under, dual-flowpath turbine-based combined cycle inlet, designed to feed a Dual-Mode Scramjet (DMSJ) combustor. While the performance of the low-speed flowpath was extensively tested in a small-scale series of experiments, the full performance of the high-speed flowpath had not yet been assessed. Therefore, numerical simulations were completed for the high-speed flowpath with and without back pressure at the mode-transition freestream Mach number, Mach 4. The simulation results show that massflow is maximized for a high-speed cowl angle of –5°. This gives researchers a range of high-speed cowl angles in which to concentrate their efforts: –4° to –6°. The simulations also showed that cowl angles of –4° and larger will have large corner separations along the ramp surface. Simulations were also completed for cowl angles positioned at –4°, –5°, and –6° with back pressure. For each cowl rotation angle, the high-speed isolator was fully back-pressure and showed excellent stability. In fact, the simulations showed that the high-speed flowpath stability margin is increased with further back-pressuring, such that the pressure rise moved upstream of the isolator and into the inlet without unstarting the inlet. Between six and eight back-pressured simulations were completed

for each cowl angle; these simulations fully characterized the high-speed flowpath under back pressure. Simulations also showed that the high-speed flowpath with a fully back-pressured isolator could withstand a 0.1 reduction in freestream Mach number. The data helped researchers plan for LIMX experiments, providing insight into the operable limits of the high-speed flowpath.

References

1. Mansour, N. N., Pittmann, J. L., and Olson, L. E., "Fundamental Aeronautics Hypersonics Project: Overview," AIAA Paper 2007-4263, June 2007.
2. Beckel, S. A., Garrett, J. L., and Gettinger, C. G., "Technologies for Robust and Affordable Scramjet Propulsion," AIAA Paper 2006-7980, Nov. 2006.
3. Auslender, A. H., Suder, K. L., Thomas, S. R., "An Overview of the NASA FAP Hypersonics Project Airbreathing Propulsion Research," AIAA Paper 2009-7277, Oct. 2009.
4. Curran, E. T., and Stull, F. D., U.S. Patent 3,667,233, "Dual Mode Supersonic Combustion Ramjet Engine," June 1972.
5. Foster, R. W., Escher, W. J. D., and Robinson, J. W., "Studies of an Extensively Axisymmetric Rocket Based Combined Cycle (RBCC) Engine Powered SSTO Vehicle," AIAA Paper 89-2294, July 1989.
6. Walker, S., Tang, M., and Mamplata, C., "TBCC Propulsion for a Mach 6 Hypersonic Airplane," AIAA Paper 2009-7238, July 2009.
7. Saunders, J. D., Slater, J. W., Dippold, V., Lee, J., Sanders, B. W., and Weir, L. J., "Inlet Mode Transition Screening Test for a Turbine-Based Combined-Cycle Propulsion System," JANNAF Propulsion Meeting, Boston, Massachusetts, May 2008.
8. Saunders, J. D., Slater, J. W., Dippold, V., Sanders, B. W., and Weir, L. J., "Inlet Research Status for a Large-Scale Turbine-Based Combined-Cycle Engine Testbed," JANNAF Propulsion Meeting, San Diego, California, Dec. 2009.
9. Soeder, R. H., Roeder, J. W., Linne, A. A., and Panek, J. W., "User Manual for NASA Glenn 10- by 10-Foot Supersonic Wind Tunnel," NASA/TM-2004-212697, May 2004.
10. Sanders, B. W. and Weir, L. J., "Aerodynamic Design of a Dual-Flow Mach 7 Hypersonic Inlet System for a Turbine-Based Combined-Cycle Hypersonic Propulsion System," NASA/CR-2008-215214, May 2008.
11. Emami, S., Trexler, C. S., Auslender, A. H., Weidner, J. P., "Experimental Investigation of Inlet-Combustor Isolators for a Dual-Mode Scramjet at a Mach Number of 4," NASA/TP-3502, May 1995.
12. Smart, M. K., and Trexler C. A., "Mach 4 Performance of Hypersonic Inlet with Rectangular-to-Elliptical Shape Transition," *Journal of Propulsion and Power*, Vol. 20, No. 2, pp. 288-293, Mar. 2004.
13. Weir, L. J. and Sanders, B. W., "Investigation of a Two-Dimensional, Mixed-Compression Mach 5.0 Inlet," NASA/CR-2004-213122, July 2004.
14. Towne, C. E., "Wind-US Users Guide, Version 2.0," NASA/TM-2009-215804, Oct. 2009.
15. Georgiadis, N. J., Yoder, D. A., Towne, C. S., Engblom, W. A., Bhagwandin, V. A., Power, G. D., Lankford, D. W., Nelson, C. C., "Wind-US Code Physical Modeling Improvements to Complement Hypersonic Testing and Evaluation," AIAA Paper 2009-193, Jan. 2009.
16. Menter, F. R., "Two-Equation Eddy Viscosity Turbulence Models for Engineering Applications," *AIAA Journal*, Vol. 32, No. 8, pp. 1598-1605, Jan. 1994.
17. Georgiadis, N. J., Dudek, J. C., and Tierney, T., "Grid Resolution and Turbulent Inflow Boundary Conditions for NPARC Calculations," AIAA Paper 95-2613, July 1995.
18. Dudek, J. C., Georgiadis, N. J., and Yoder, D. A., "Calculation of turbulent subsonic diffuser flows using the NPARC Navier-Stokes code," AIAA Paper 96-0497, Jan. 1996.
19. Slater, J. W., "Verification Assessment of Flow Boundary Conditions for CFD Analysis of Supersonic Inlet Flows," AIAA Paper 2001-3882, July 2001.
20. Slater, J. W. and Saunders, J. D., "CFD Simulation of Hypersonic TBCC Inlet Mode Transition," AIAA Paper 2009-7349, Oct. 2009.

TABLE 1.—GRID CONVERGENCE: MASSFLOW AND MASS-AVERAGED TOTAL PRESSURE AT AIP

Grid Level Solution	Coarse		Medium		Fine	
	Actual	Delta (%)	Actual	Delta (%)	Actual	Delta (%)
Mass flow (lbm/s)	3.525	--	3.566	1.15	3.585	0.55
p_0 (psi)	13.897	--	14.253	2.56	14.163	–0.63

TABLE 2.—AIP PRESSURE, PRESSURE DISTORTION, AND PERCENT CHANGE WITH RESPECT TO THE NORMAL SHOCK PRESSURE RISE FOR –4° HIGH-SPEED COWL ANGLE AND VARIABLE CONVERGING-DIVERGING NOZZLE SECTION

$p_{AIP}/p_{iso,ref}$	0.728	1.57	1.78	1.94	2.18	2.27
C-D nozzle throat area (%)	100	90	88	86	83	81
Max pressure (psi)	3.4502	7.1533	8.0874	8.7311	9.4053	9.8949
Min pressure (psi)	2.7995	6.188	7.078	7.677	8.5074	9.1144
Mass-average static pressure (psi)	3.0278	6.5727	7.4383	8.0889	8.8636	9.4224
AIP static pressure distortion (%)	21.49	14.69	13.57	13.03	10.13	8.28
p, normal shock (%)	33.0	71.3	80.8	87.98	96.6	102.9
p_0, normal shock (%)	89.4	86.0	86.3	89.1	89.7	86.7

TABLE 3.—AIP PRESSURE, PRESSURE DISTORTION, AND PERCENT CHANGE WITH RESPECT TO THE NORMAL SHOCK PRESSURE RISE FOR –5° HIGH-SPEED COWL ANGLE AND VARIABLE CONVERGING-DIVERGING NOZZLE SECTION

$p_{AIP}/p_{iso,ref}$	0.781	0.782	1.62	2.28	2.72	2.86
C-D nozzle throat area (%)	100	88	86	83	80	78
Max pressure (psi)	3.6053	3.6571	7.0401	9.8321	11.3896	12.0577
Min pressure (psi)	2.8991	2.884	5.7892	8.4448	10.4172	11.0837
Mass-average static pressure (psi)	3.1696	3.1821	6.611	9.1899	10.956	11.5224
AIP static pressure distortion (%)	22.28	24.30	18.92	15.10	8.88	8.45
p, normal shock (%)	25.8	25.8	53.3	75.3	90.0	94.6
p_0, normal shock (%)	93.6	95.2	88.1	83.8	82.9	84.5

TABLE 4.—AIP PRESSURE, PRESSURE DISTORTION, AND PERCENT CHANGE WITH RESPECT TO THE NORMAL SHOCK PRESSURE RISE FOR –6° HIGH-SPEED COWL ANGLE AND VARIABLE CONVERGING-DIVERGING NOZZLE SECTION

$p_{AIP}/p_{iso,ref}$	0.841	0.833	1.45	1.96	2.38	2.92	3.17	3.46
C-D nozzle throat area (%)	100	88	86	85	83	80	78	75
Max pressure (psi)	3.1143	3.1179	5.7533	7.1458	8.6306	10.2293	11.1612	11.9976
Min pressure (psi)	2.6195	2.5438	3.9895	5.7379	7.3762	9.3824	10.223	11.2154
Mass-average static pressure (psi)	2.7764	2.7729	4.9655	6.4834	7.9968	9.766	10.5917	11.5116
AIP static pressure distortion (%)	17.82	20.70	35.52	21.72	15.69	8.67	8.86	6.79
p, normal shock (%)	23.57	23.4	43.8	55.0	67.7	82.7	89.6	97.5
p_0, normal shock (%)	97.65	98.3	92.1	90.1	87.5	83.9	84.0	85.2

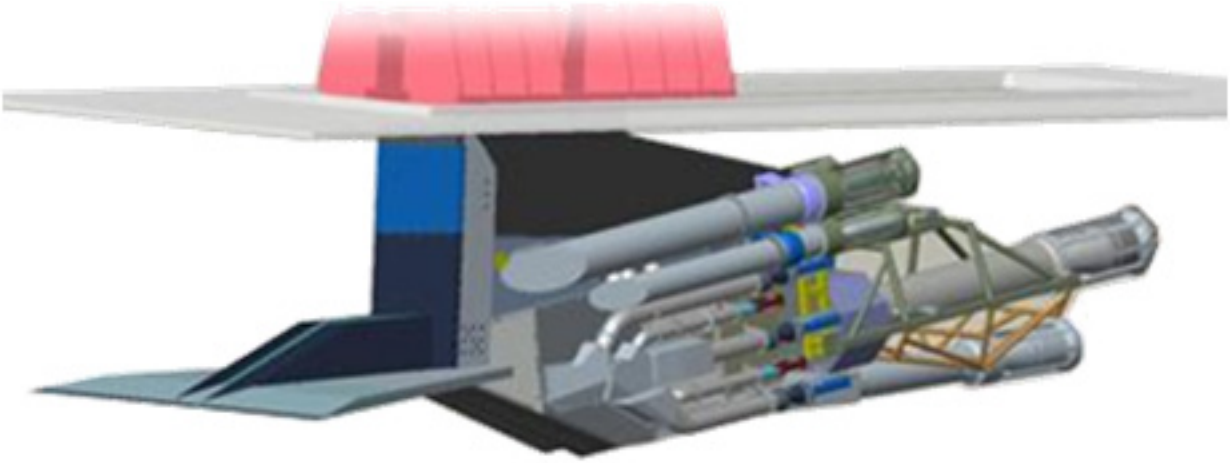

Figure 1.—CAD-generated image of the LIMX inlet model mounted in the wind tunnel.

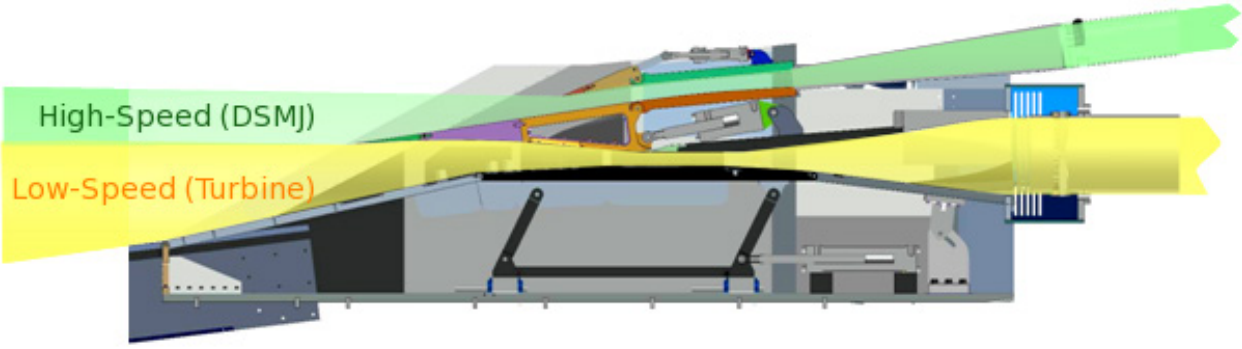

Figure 2.—Inverted LIMX dual-flowpath inlet with the splitter positioned to allow airflow into both flowpaths.

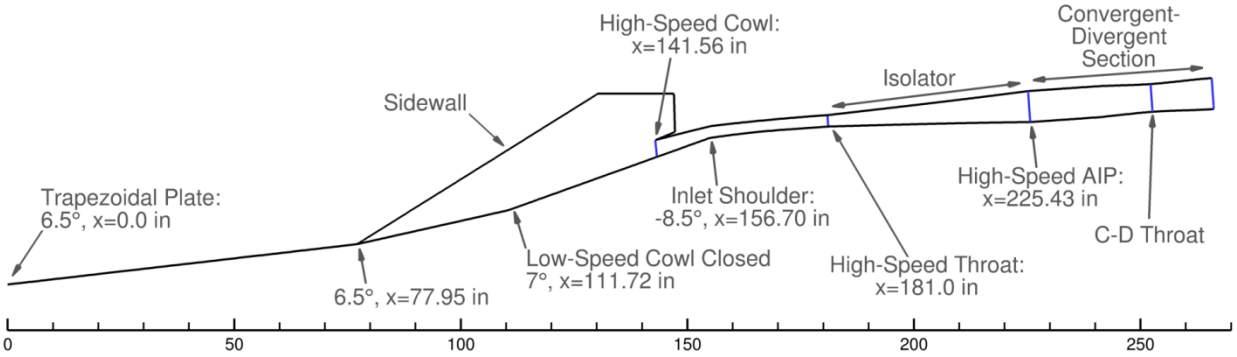

Figure 3.—Schematic of simplified LIMX inlet high-speed flowpath used for CFD (–6° high-speed cowl, 80 percent A_t/A_{AIP}).

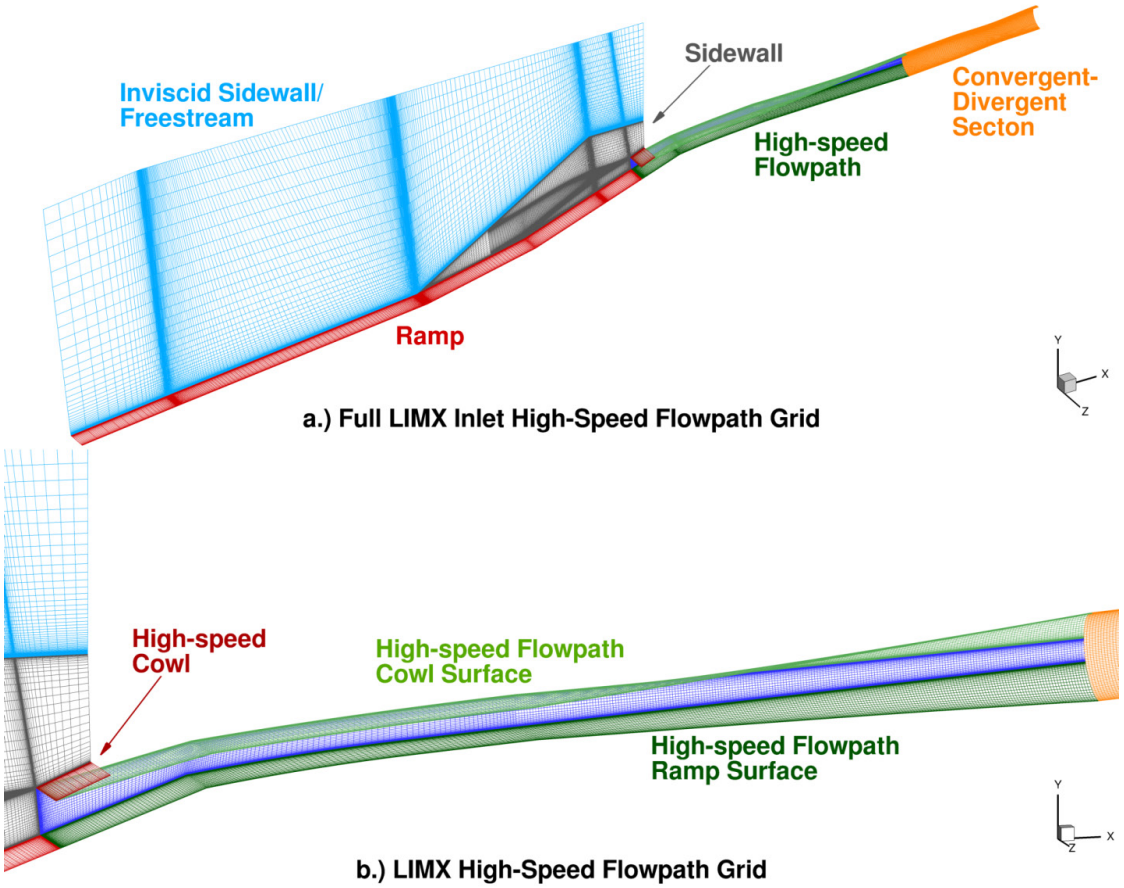

Figure 4.—LIMX high-speed inlet grid (–6° high-speed cowl, 80 percent A_t/A_{AIP}).

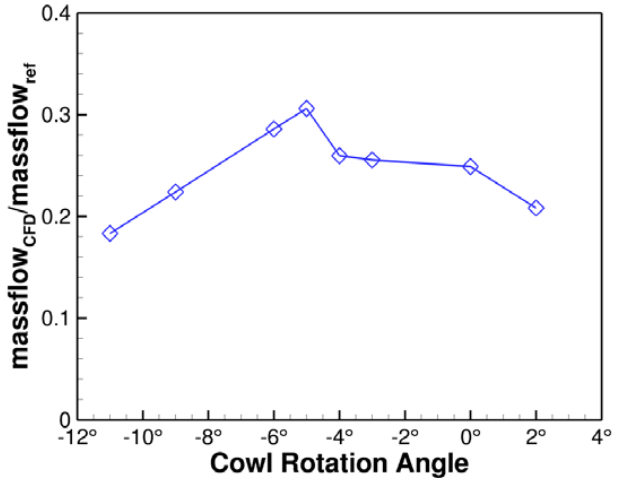

Figure 5.—LIMX high-speed flowpath massflow at the AIP with no back pressure.

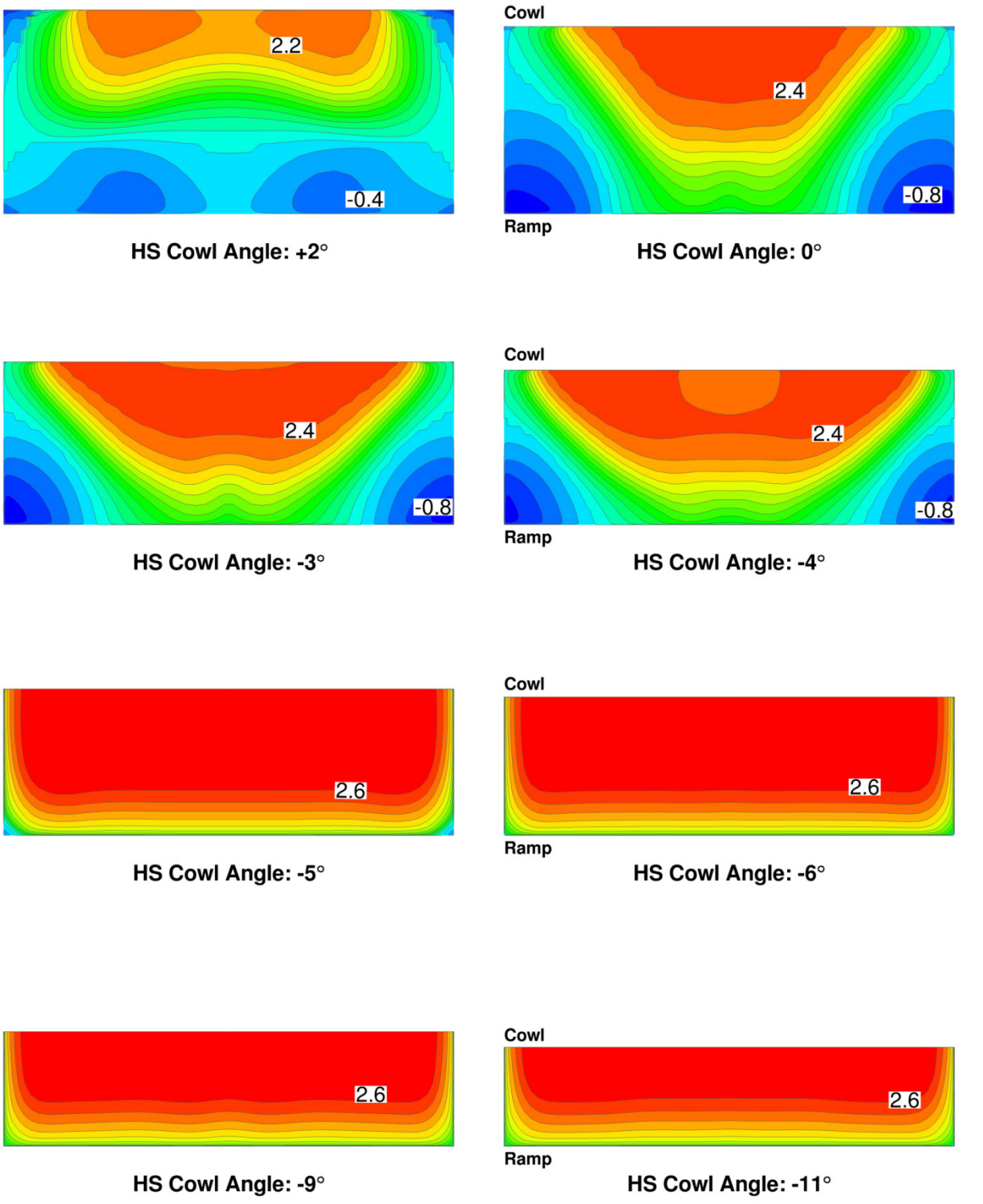

Figure 6.—Signed Mach number contours at LIMX high-speed flowpath entrance with the high-speed cowl set at different angles and no back pressure.

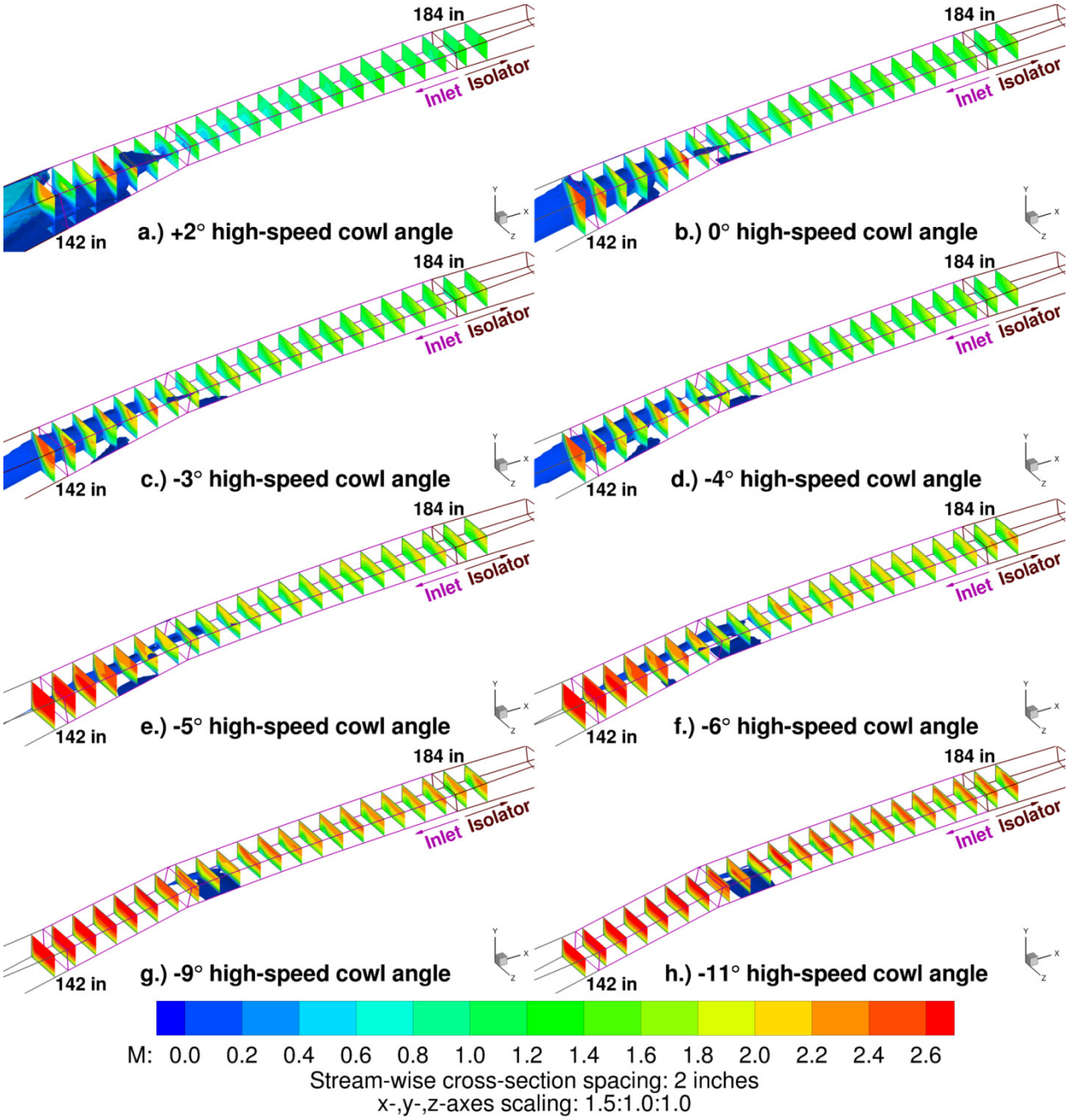

Figure 7.—Mach number contours through LIMX high-speed flowpath without back pressure.

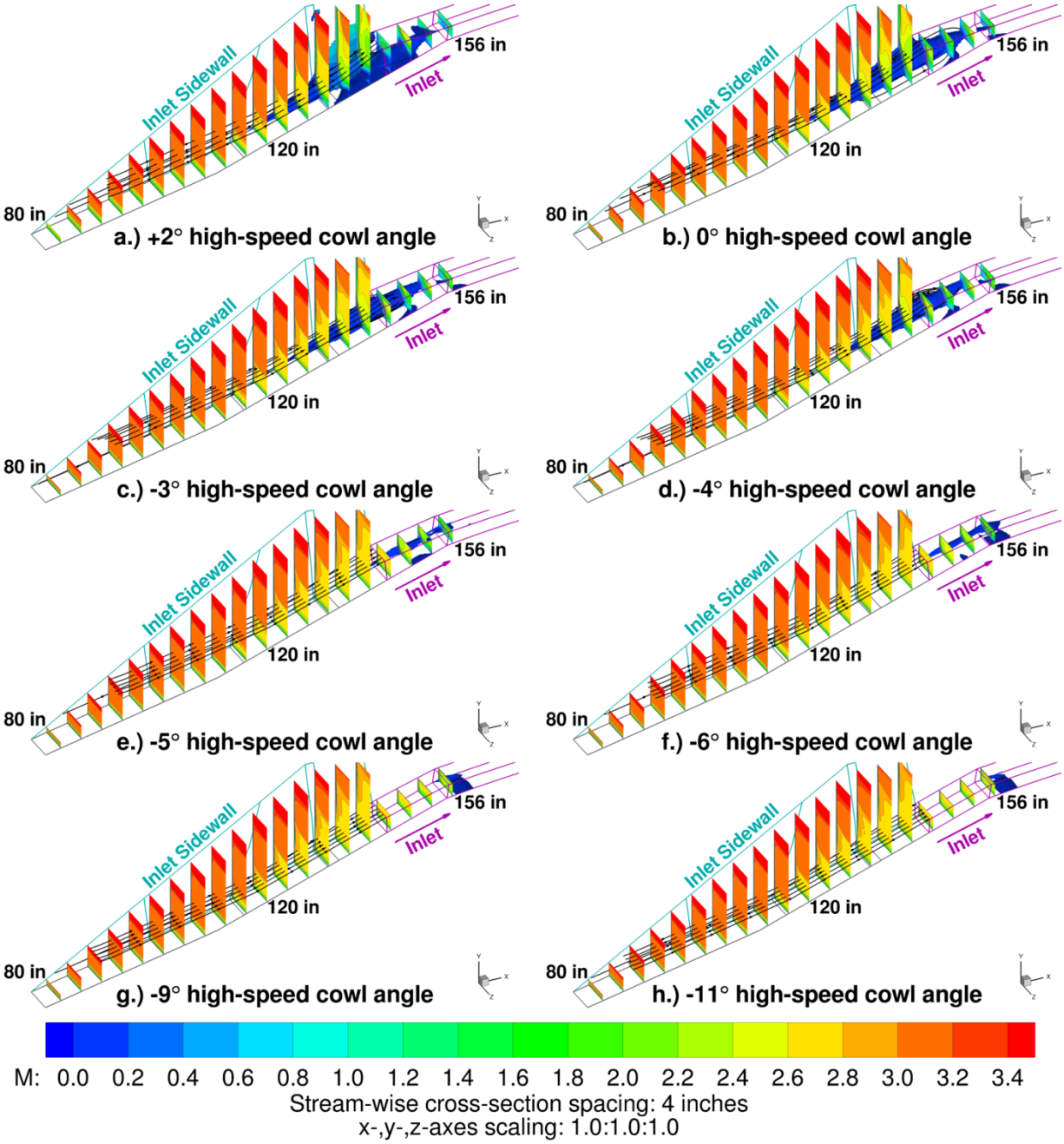

Figure 8.—Mach number contours and stagnation streamlines over ramp of LIMX high-speed flowpath without back pressure.

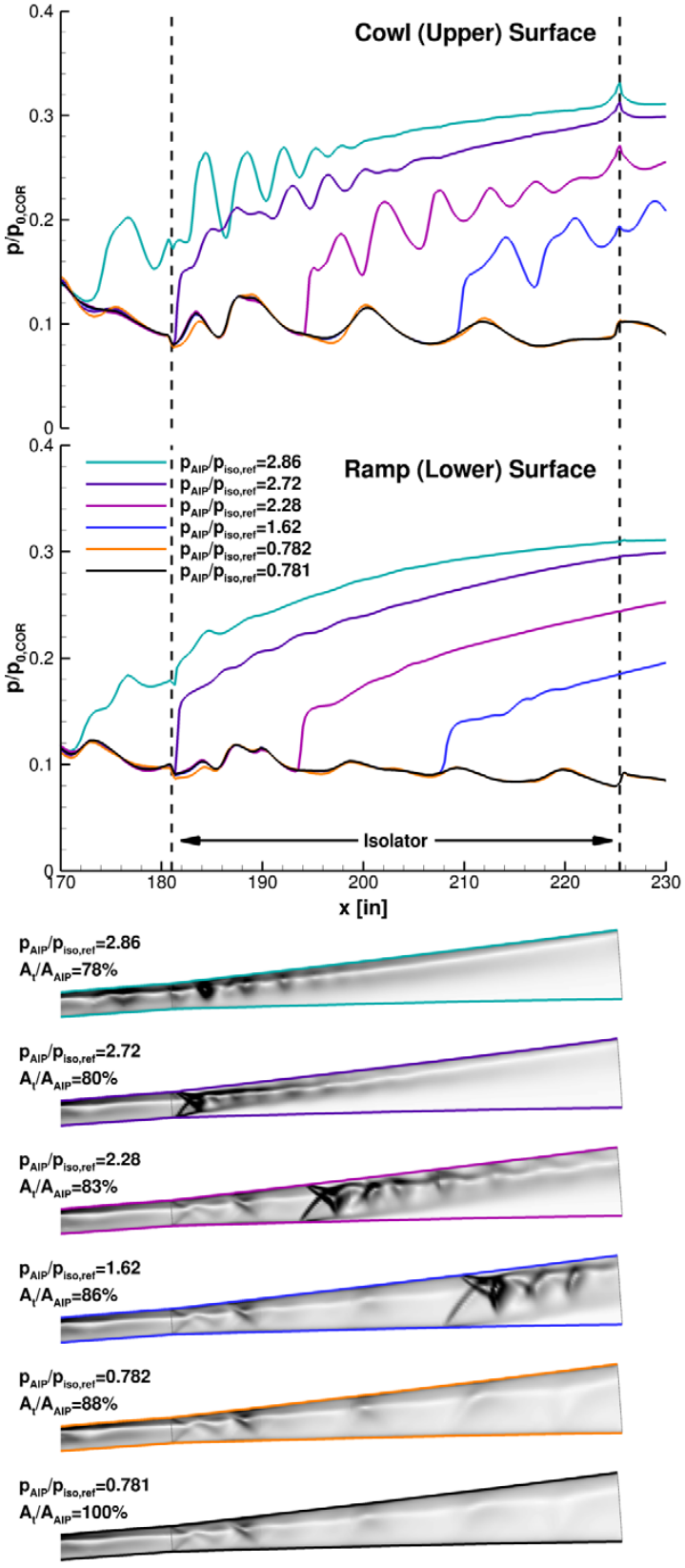

Figure 9.—Simulated LIMX isolator surface pressure and schlieren images with the high-speed cowl positioned at –5°.

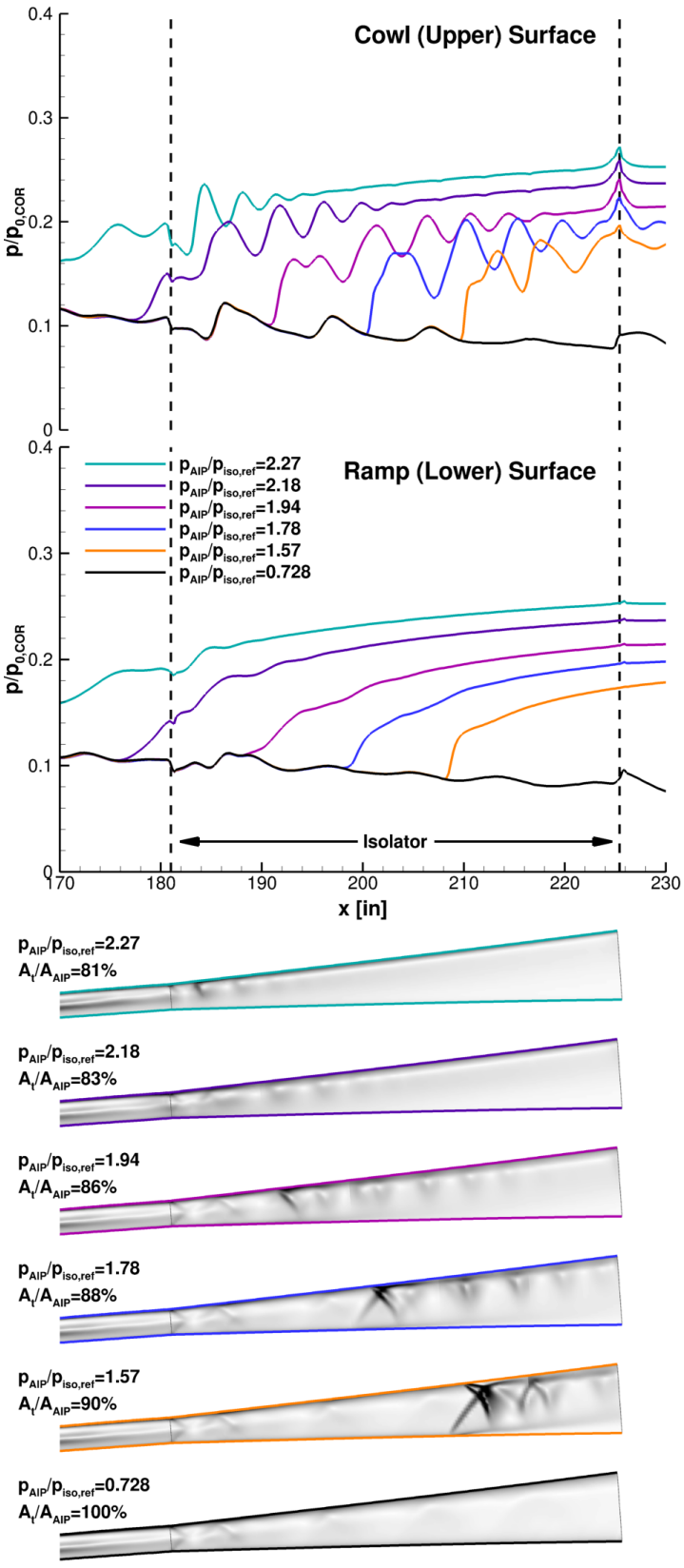

Figure 10.—Simulated LIMX isolator surface pressure and schlieren images with the high-speed cowl positioned at –4°.

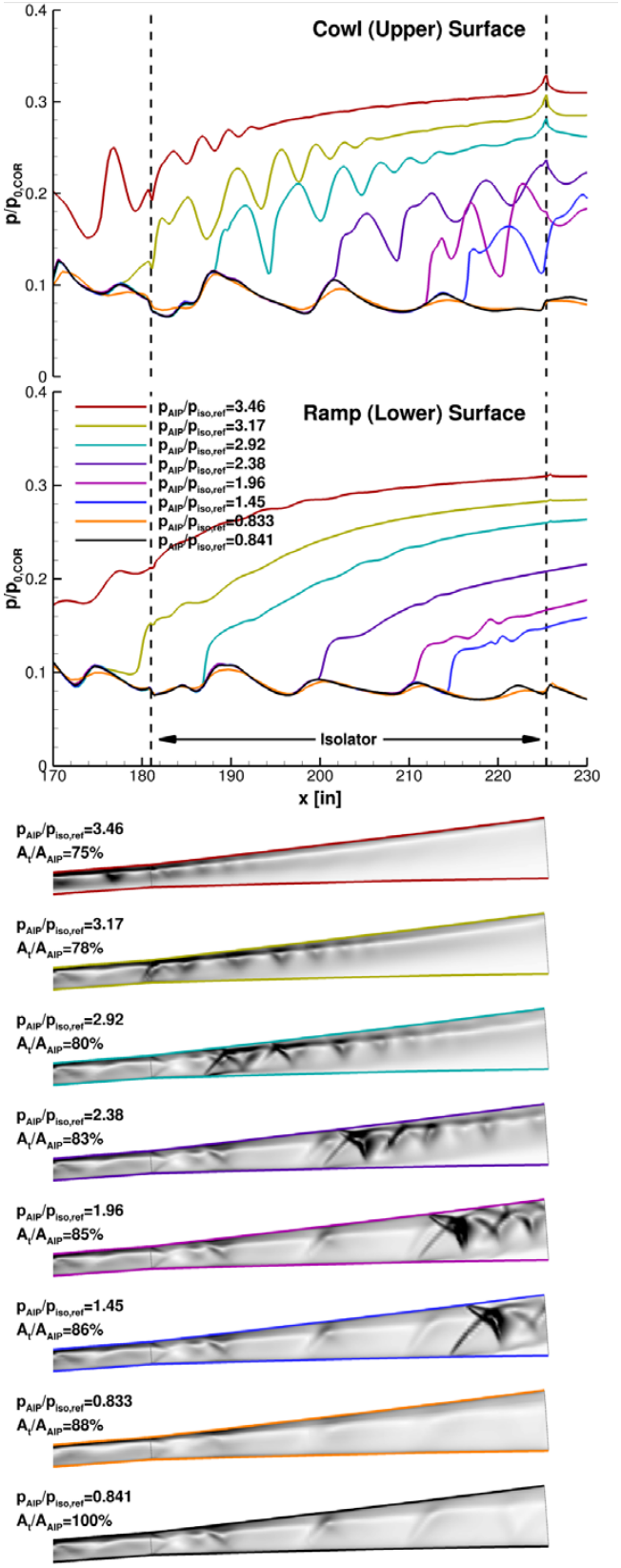

Figure 11.—Simulated LIMX isolator surface pressure and schlieren images with the high-speed cowl positioned at –6°.

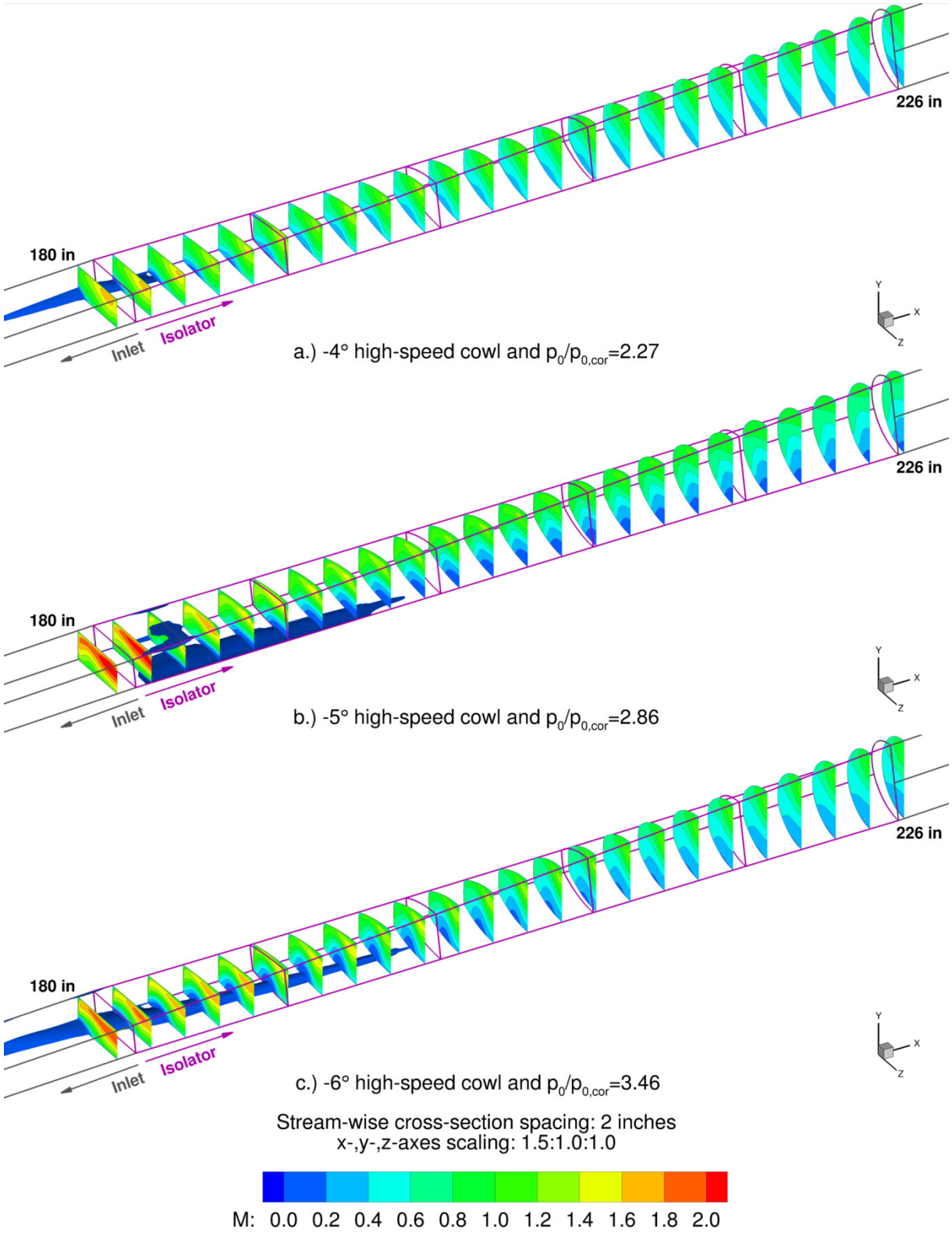

Figure 12.—Mach number contours through LIMX isolator.

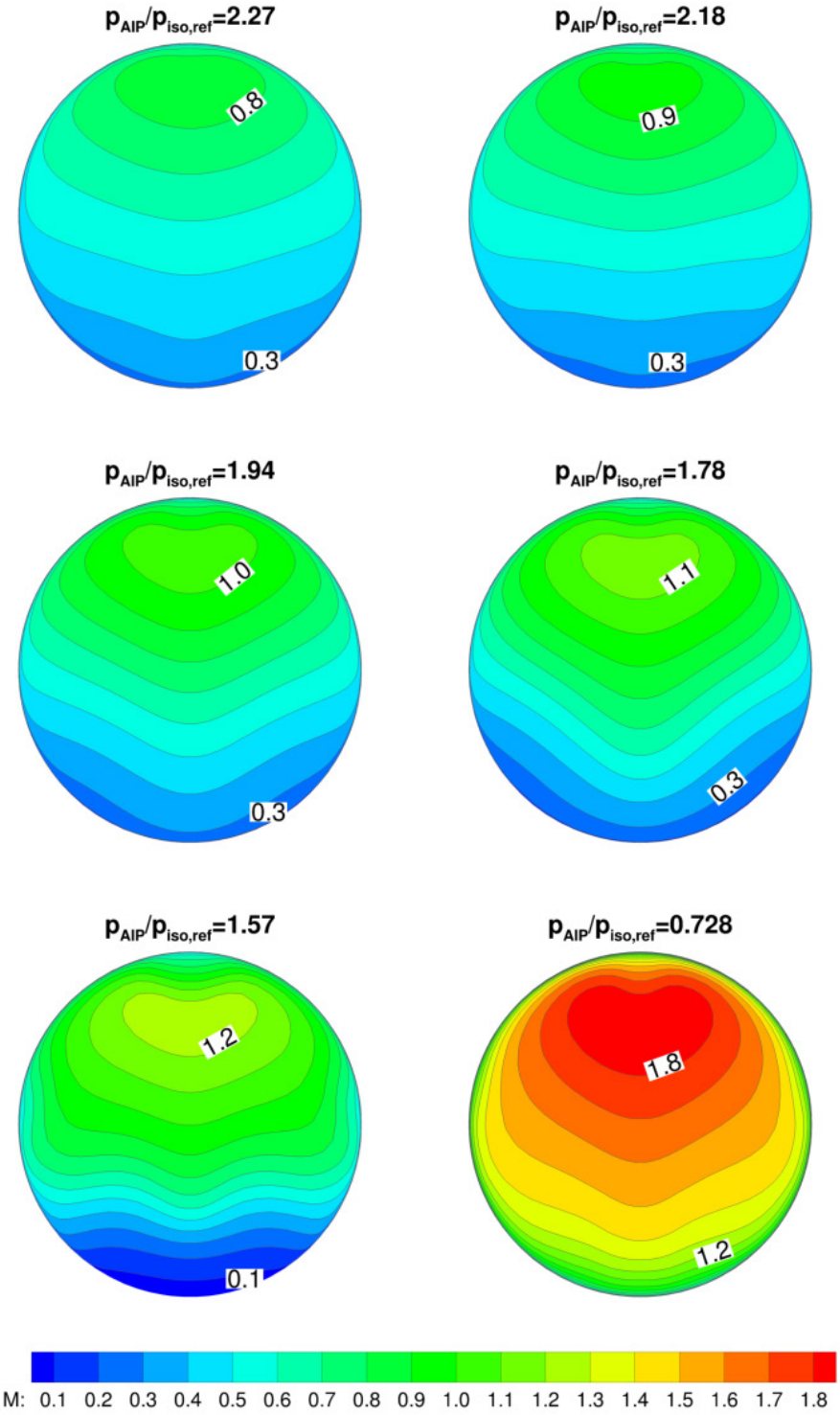

Figure 13.—Mach number contours at AIP of LIMX high-speed flowpath with –4° cowl angle and back pressure.

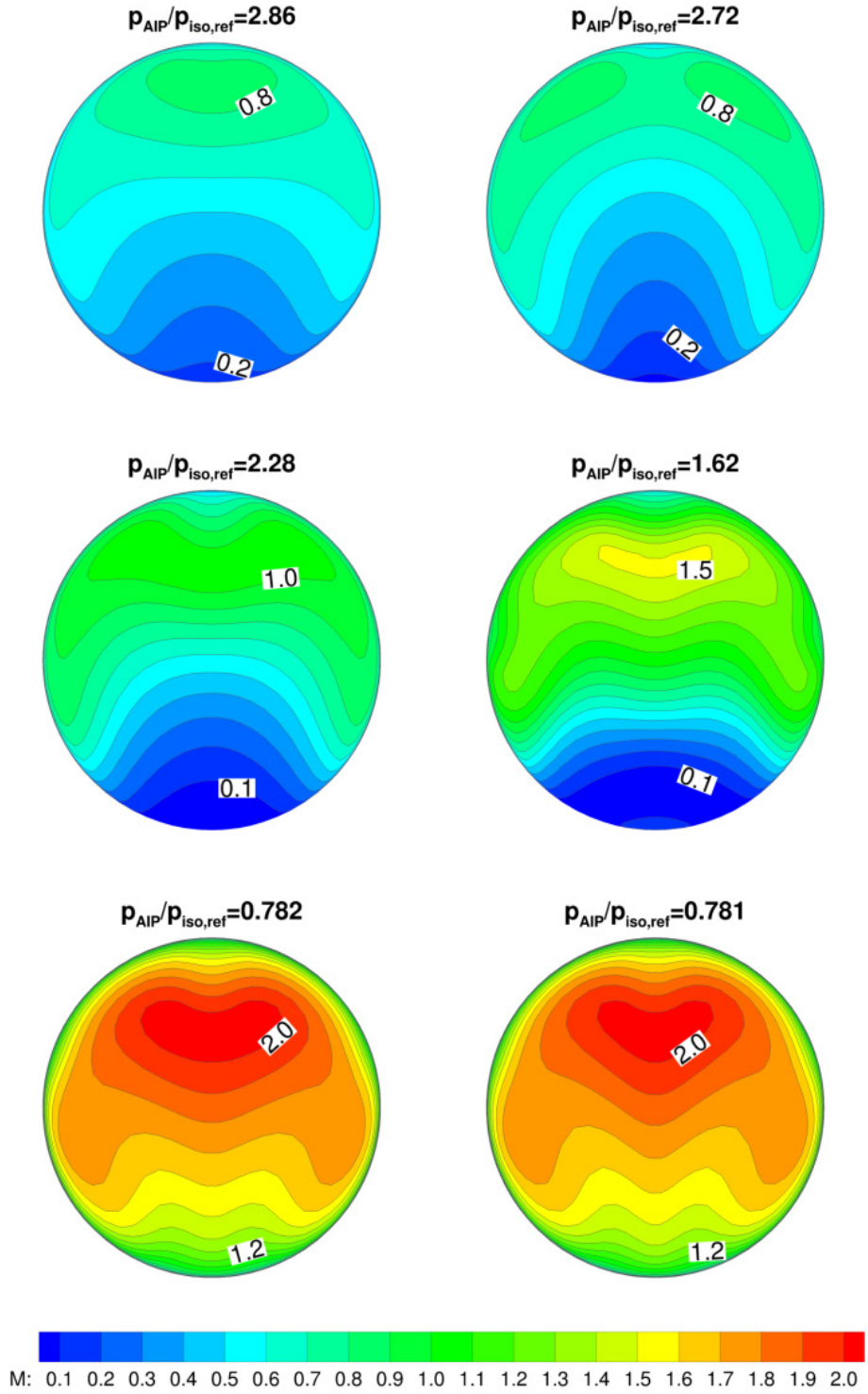

Figure 14.—Mach number contours at AIP of LIMX high-speed flowpath with –5° cowl angle and back pressure.

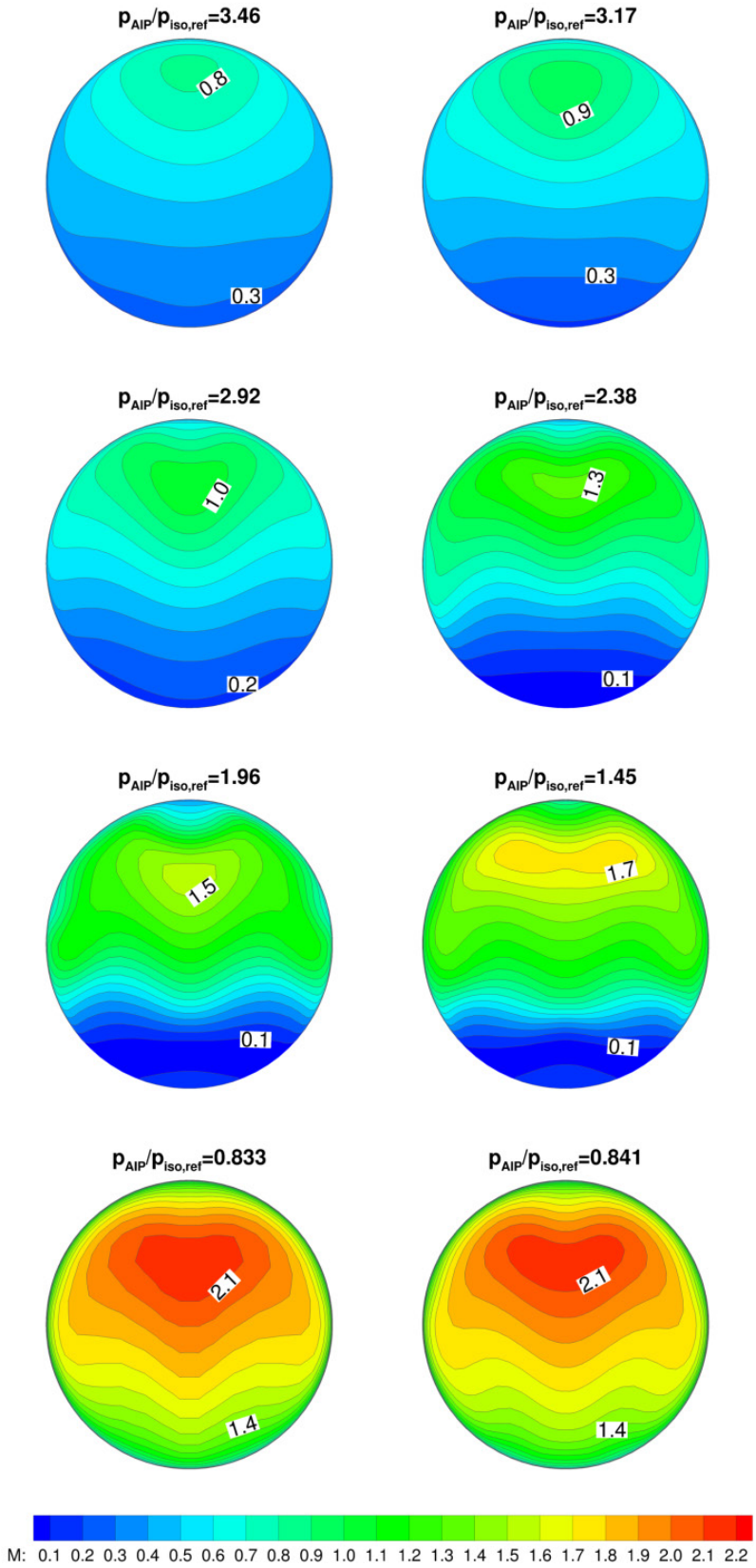

Figure 15.—Mach number contours at AIP of LIMX high-speed flowpath with –6° cowl angle and back pressure.

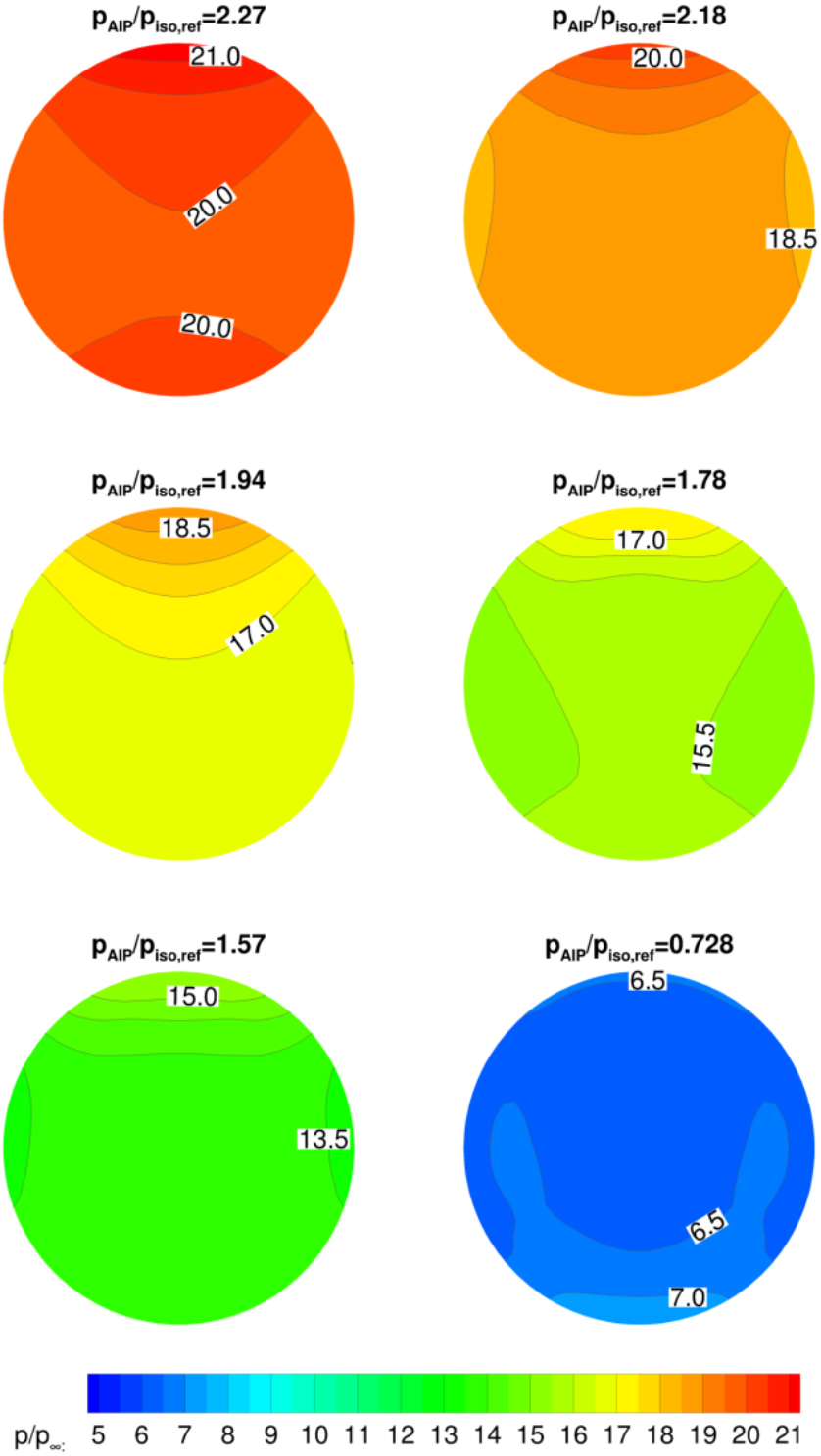

Figure 16.—Static pressure contours at AIP of LIMX high-speed flowpath with –4° cowl angle and back pressure.

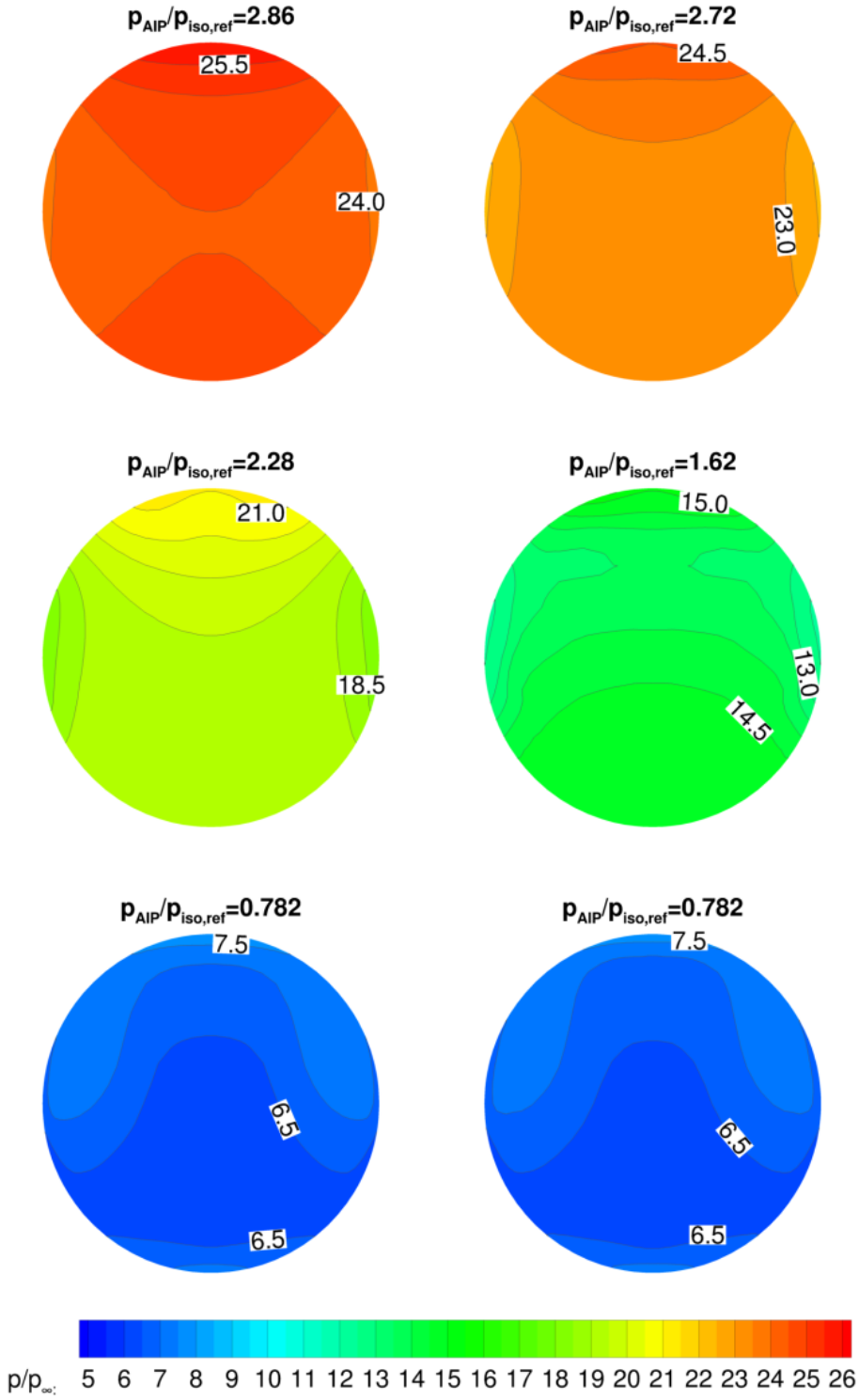

Figure 17.—Static pressure contours at AIP of LIMX high-speed flowpath with –5° cowl angle and back pressure.

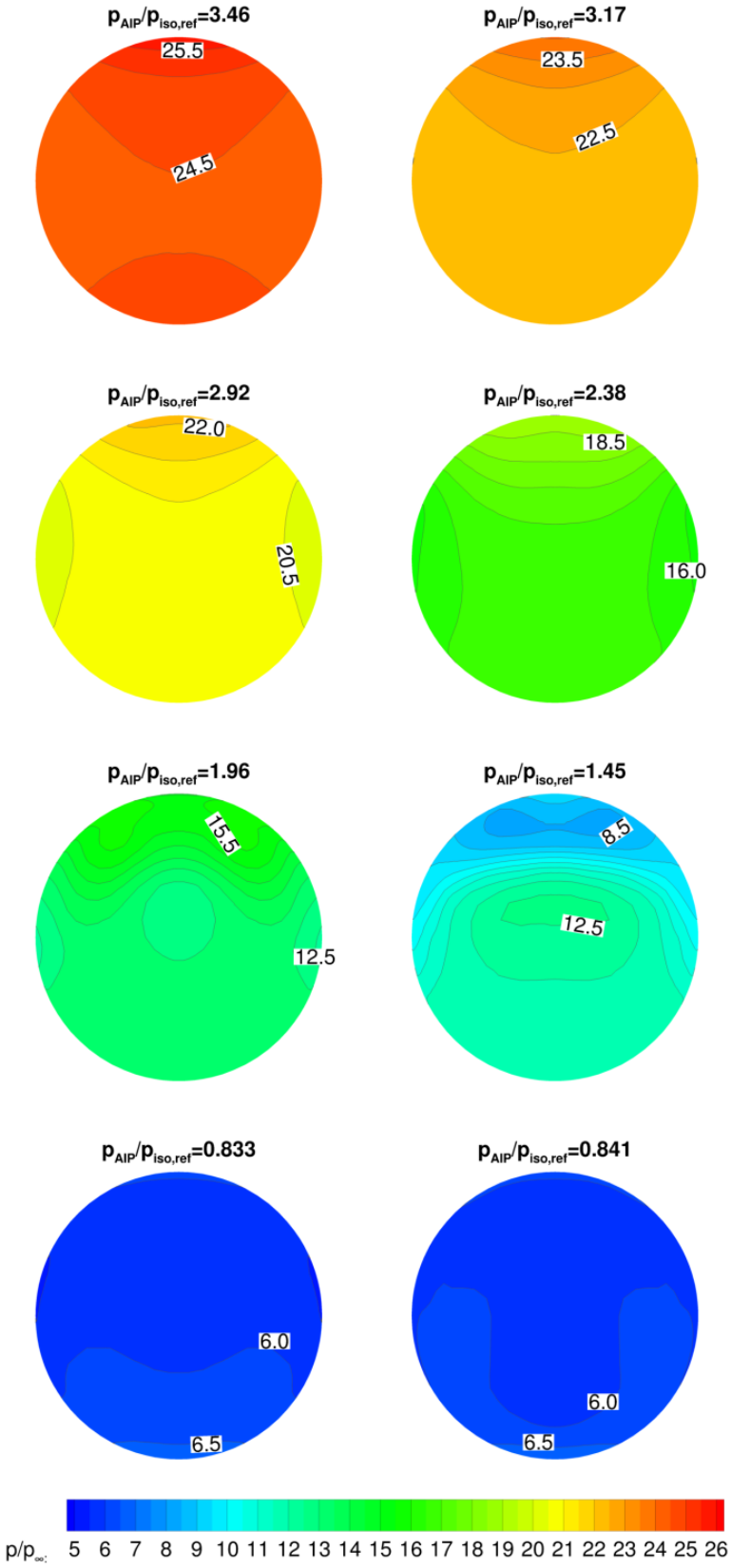

Figure 18.—Static pressure contours at AIP of LIMX high-speed flowpath with –6° cowl angle and back pressure.

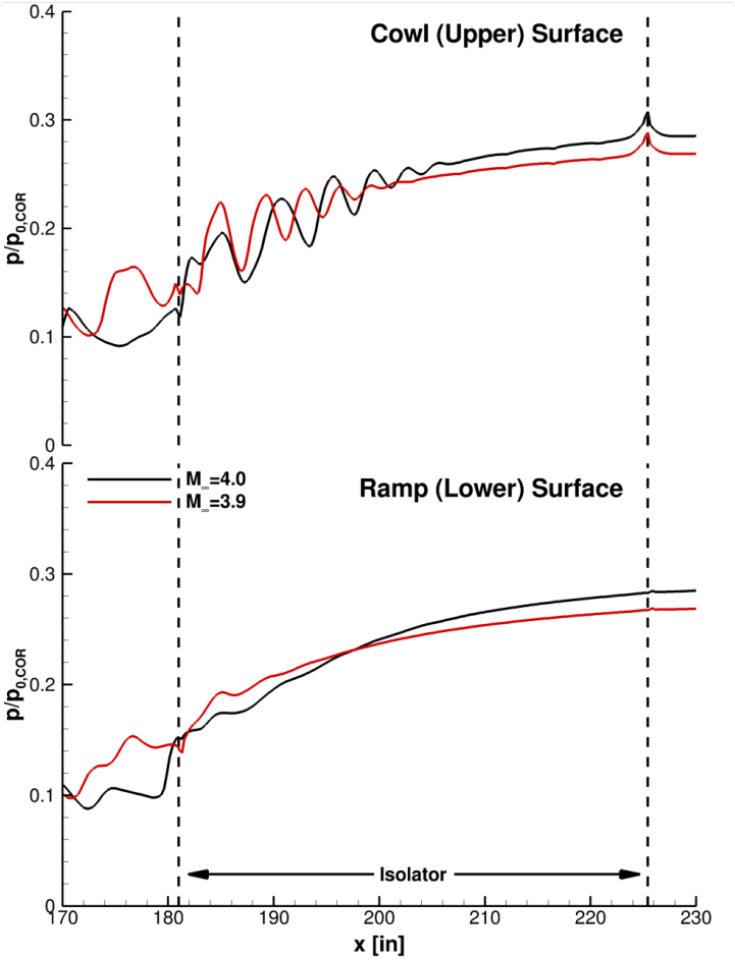

Figure 19.—LIMX isolator surface pressure for –6° cowl angle and varying freestream Mach number.

REPORT DOCUMENTATION PAGE	Form Approved OMB No. 0704-0188

1. REPORT DATE *(DD-MM-YYYY)*	2. REPORT TYPE	3. DATES COVERED *(From - To)*
01-01-2012	Technical Memorandum	

4. TITLE AND SUBTITLE
Computational Analyses of the LIMX TBCC Inlet High-Speed Flowpath

5a. CONTRACT NUMBER

5b. GRANT NUMBER

5c. PROGRAM ELEMENT NUMBER

6. AUTHOR(S)
Dippold, Vance, F., III

5d. PROJECT NUMBER

5e. TASK NUMBER

5f. WORK UNIT NUMBER
WBS 599489.02.07.03.07.11.02

7. PERFORMING ORGANIZATION NAME(S) AND ADDRESS(ES)
National Aeronautics and Space Administration
John H. Glenn Research Center at Lewis Field
Cleveland, Ohio 44135-3191

8. PERFORMING ORGANIZATION REPORT NUMBER
E-17900

9. SPONSORING/MONITORING AGENCY NAME(S) AND ADDRESS(ES)
National Aeronautics and Space Administration
Washington, DC 20546-0001

10. SPONSORING/MONITOR'S ACRONYM(S)
NASA

11. SPONSORING/MONITORING REPORT NUMBER
NASA/TM-2012-217219

12. DISTRIBUTION/AVAILABILITY STATEMENT
Unclassified-Unlimited
Subject Categories: 01, 02, and 07
Available electronically at http://www.sti.nasa.gov
This publication is available from the NASA Center for AeroSpace Information, 443-757-5802

13. SUPPLEMENTARY NOTES

14. ABSTRACT
Reynolds-Averaged Navier-Stokes (RANS) simulations were performed for the high-speed flowpath and isolator of a dual-flowpath Turbine-Based Combined-Cycle (TBCC) inlet using the Wind-US code. The RANS simulations were performed in preparation for the Large-scale Inlet for Mode Transition (LIMX) model tests in the NASA Glenn Research Center (GRC) 10- by 10-ft Supersonic Wind Tunnel. The LIMX inlet has a low-speed flowpath that is coupled to a turbine engine and a high-speed flowpath designed to be coupled to a Dual-Mode Scramjet (DMSJ) combustor. These RANS simulations were conducted at a simulated freestream Mach number of 4.0, which is the nominal Mach number for the planned wind tunnel testing with the LIMX model. For the simulation results presented in this paper, the back pressure, cowl angles, and freestream Mach number were each varied to assess the performance and robustness of the high-speed inlet and isolator. Under simulated wind tunnel conditions at maximum inlet mass flow rates, the high-speed flowpath pressure rise was found to be greater than a factor of four. Furthermore, at a simulated freestream Mach number of 4.0, the high-speed flowpath and isolator showed stability for freestream Mach number that drops 0.1 Mach below the design point. The RANS simulations indicate the yet-untested high-speed inlet and isolator flowpath should operate as designed. The RANS simulation results also provided important insight to researchers as they developed test plans for the LIMX experiment in GRC's 10- by 10-ft Supersonic Wind Tunnel.

15. SUBJECT TERMS
Turbine-based combined-cycle; Hypersonic; Inlet; Isolator; Inlet mode transition; CFD

16. SECURITY CLASSIFICATION OF:			17. LIMITATION OF ABSTRACT	18. NUMBER OF PAGES	19a. NAME OF RESPONSIBLE PERSON
a. REPORT	b. ABSTRACT	c. THIS PAGE			STI Help Desk (email:help@sti.nasa.gov)
U	U	U	UU	34	19b. TELEPHONE NUMBER *(include area code)* 443-757-5802